Ship Detection by the RADARSAT SAR: Validation of Detection Model Predictions

by P.W. Vachon, J.W.M. Campbell, C.J. Bjerkelund, F.W. Dobson, M.T. Rey

Résumé

Nous avons utilisé une approche statistique de détection de cibles ponctuelles sur fond bruité pour caractériser la performance prévue du RSO de RADARSAT (bande C, Polarisation HH) pour la détection des navires. Cette technique sera égale-ment utilisée pour comparer la performance des divers modes et faisceaux du RSO de RADARSAT pour la détection des navires. La détection de navires de plus petite dimension est possible lorsque la vitesse du vent est plus faible, que l'angle d'incidence est plus fort ou que la résolution est plus fine. Le mode ScanSAR à faisceau étroit distal est pressenti comme étant le meilleur compromis entre la couverture spatiale et la probabilité de détection. Nous présentons une validation quan-titative de ces modèles de prédiction selon les données obtenues lors d'une campagne qui a eu lieu au large de Halifax N.-E. au cours des mois de mars et avril 1996. À l'aide d'instruments sur bouées, des mesures du vent et des vagues ont été prises au moment de l'acquisition d'images RSO de RADARSAT, alors que plusieurs navires connus étaient présents dans la scène. Nous présentons des validations de plusieurs des paramètres clés du modèle et notamment les paramètres concernant notre modèle hybride de section transversale équivalente océanique en bande C, polarisation HH, de la densité de probabilité de l'image et de la signature radar des navires.

Summary

A statistical approach to point target detection in a clutter background is used to delineate the expected performance of the RADARSAT SAR (C-band HH polarization) for ship detection, and to compare the expected ship detection performance for the various RADARSAT SAR beam modes. Smaller ships may be detected with decreasing wind speed, increasing incidence angle, and finer resolution. ScanSAR Narrow Far is expected to be a good compromise between spatial coverage and detection probability. We present a quantitative validation of these model predictions based upon data acquired during a RADARSAT SAR ship detection/validation field program, which was held in March/April 1996 off the coast of Halifax, Nova Scotia. The program included buoy measurements of wind and wave conditions and RADARSAT SAR passes with known ships in each scene. We present validation of some of the model's key assumptions, in particular those concerning our hybrid C-band HH polarization ocean cross-section model, image probability density function, and ship radar signatures.

Introduction

Ship detection by the RADARSAT synthetic aperture radar (SAR) has become a topic of considerable interest since there could be a significant commercial market for this type of information (Tack and Nazarenko, 1996).

There has already been considerable work done on ship and other target detection in a radar clutter background, especially in the context of existing SAR systems. Much of the literature on this topic is presumably classified. However, Gray *et al.* (Gray *et al*., 1984) worked out generic target detection probabilities while Freeman *et al*. (Freeman *et al*., 1986) showed scatterometer results which well-illustrate the ship detection problem: as the wind speed U increases, the ocean clutter (i.e. the normalized radar cross section s°) increases and ship detectability is degraded. They also showed how detectability improves with increasing incidence angle u since the ocean clutter decreases while the ship signature remains largely independent of incidence angle.

The most relevant recent results to quantifying the RADARSAT SAR's ship detection capability are based upon the extensive experience with ERS-1 SAR data. The C-band VV polarization images from the ERS-1 SAR have been used on a pre-operational basis in Norway with considerable success (Wahl *et al*., 1993). The Norwegian approach is to use the ship signature as the primary ship indicator, and the ship wake as a secondary indicator which could supply additional information about the ship and its velocity (Eldhuset, 1996). However, experience with ERS-1 and Seasat SARs indicates that wakes are not seen for roughly 37 % of all ship targets. This figure is expected to be larger for RADARSAT which will have a lower signal to-noise ratio due to its HH polarization. Thus, the key

- P.W. Vachon and C.A. Bjerkelund are with the Canada Centre for Remote Sensing, 588 Booth St., Ottawa, Ont.K1A 0Y7, Phone: 613 995-1575, Fax: 613 947-1385, E-mail: paris.vachon@ccrs.nrcan.gc.ca
- J.W.M. Campbell is under contract to CCRS from Intermap, 2 Gurdwara Rd., Suite 20, Nepean, Ont. K2E 1A2
- F.W. Dobson is with the Bedford Institute of Oceanography, P.O. Box 1006, Dartmouth, N.S. B2Y 4A2
- M.T. Rey is with the Defence Research Establishment Ottawa, 3701 Carling Ave., Ottawa, Ont. K1A 0Z4

issue for RADARSAT is bright target detection (for the ship) rather than linear feature detection (for the ship wake).

In order to compare the RADARSAT SAR's expected performance with that of the ERS-1 SAR, we consider the key differences between the two systems. While both are C-band instruments with comparable radiometric and spatial resolutions (for the RADARSAT SAR standard beams), the ERS-1 SAR has VV polarization and a steep incidence angle, while the RADARSAT SAR has HH polarization and the potential for much shallower incidence angles with its variable acquisition swath. It is well known that HH polarization has a lower ocean clutter signature than does VV. Also, as noted previously, the clutter level will decrease with increasing incidence angle. Thus, we expect that, for similar wind and wave conditions and image resolutions, the RADARSAT SAR will offer a better ship detection capability than the ERS-1 SAR. One objective of this work is to better quantify this expectation.

A statistical model for quantifying RADARSAT's ship detection performance was developed in the RADARSAT pre-launch period (Vachon, 1995). The model was developed based upon experience with ERS-1 SAR data and includes ocean clutter, SAR image probability density functions, and ship cross section elements. This model and its predictions are first reviewed

A RADARSAT SAR ship detection field program was carried out off Halifax, Nova Scotia in March/April 1996. Available data include RADARSAT SAR images from various beam modes, known ships, and moored wind and wave buoys which provided excellent knowledge of the relevant local conditions. The field program data are reviewed. Calibration of the RADARSAT SAR images is then discussed. Finally, a successful validation of several of the model's key assumptions using the field program data is presented.

RADARSAT SAR SHIP DETECTION MODEL

The ship detection model considered in this paper includes assumptions about the SAR image probability density function (pdf) for ocean scenes, the relationship between radar cross section, wind speed, and geometry for C-band radars, and the relationship between a ship's size and its radar cross section. The model, as presented here, was developed prior to RADARSAT's launch using ERS-1 SAR data. Some of the model's assumptions are validated in subsequent sections using actual RADARSAT SAR data.

SAR Ocean Scene Image Statistics

The higher order SAR image moments (i.e. skewness and kurtosis) for ocean scenes are known to relate to the well-known azimuth cutoff in SAR ocean imaging (Chapron *et al.*, 1994), which in turn relates to the local wind and wave conditions (Vachon *et al*., 1994). These image moments serve to define the image pdf.

We propose the multi-look intensity K-distribution (Oliver, 1993) to describe the pdf of the SAR image intensity:

$$p(I) = \frac{2}{1}\left(\frac{LvI}{\langle I\rangle}\right)^{(L+v)/2} \frac{1}{\Gamma(L)\Gamma(v)} K_{v-L}\left[2\left(\frac{LvI}{\langle I\rangle}\right)^{1/2}\right] \quad , \quad (1)$$

where $p(I)$ is the probability of image intensity I, $\langle I\rangle$ is the mean image intensity, L is the number of statistically independent looks, v is an order parameter for the intensity modulation process, Γ is the gamma-function, and K_{v-L} is the modified Bessel-function of order $v-L$. The moments about zero for this distribution are given by

$$\langle I^m\rangle = \langle I\rangle^m \frac{\Gamma(L+m)\,\Gamma(v+m)}{L^m v^m \Gamma(L)\Gamma(v)} \quad (2)$$

These distributions are well-known and have been used extensively for modelling radar clutter statistics for the ocean surface (Trunk and George, 1979, for example). The order parameter v could represent the effect of a non-Gaussian scene on the image intensity pdf.

In the limit that $v \to \infty$, the intensity K-distribution converges to the χ-squared distribution with $2L$ degrees-of-freedom:

$$p(I) = \frac{1}{I}\left(\frac{LI}{\langle I\rangle}\right)^{L} \frac{1}{\Gamma(L)} \exp\left[-\frac{LI}{\langle I\rangle}\right] \quad (3)$$

which has moments about zero given by

$$\langle I^m\rangle = \langle I\rangle^m \frac{\Gamma(L+m)}{L^m\Gamma(L)} \quad (4)$$

This latter distribution is the well-known SAR image intensity distribution in the event of a Gaussian noise input to a SAR system.

To test the suitability of the intensity K-distribution, we consider the Pearson Diagram, in which the kurtosis is plotted against the skewness-squared. The skewness is a measure of the lack of symmetry of the pdf and is defined as the normalized third moment about the mean:

$$a_3 = \frac{m_3}{m_2^{3/2}} \quad , \quad (5)$$

while the kurtosis is a measure of the rapidity of the pdf's approach to zero and is defined as the normalized fourth moment about the mean:

$$a_4 = \frac{m_4}{m_2^2} \quad , \quad (6)$$

The required moments about the mean may be computed from the moments about zero as follows:

$$m_2 = \langle I^2\rangle - \langle I\rangle^2 \quad (7)$$

$$m_3 = \langle I^3\rangle - 3\langle I^2\rangle\langle I\rangle + 2\langle I\rangle^3 \quad (8)$$

$$m_4 = \langle I^4\rangle - 4\langle I^3\rangle\langle I\rangle + 6\langle I^2\rangle\langle I\rangle^2 - 3\langle I\rangle^4 \quad (9)$$

Based on a series of ERS-1 SAR validation field programs to the Grand Banks of Newfoundland, we have available ERS-1 SAR imagery and excellent *in situ* validation information. Here, we consider data from the ERS-1 Cal/Val campaign of Nov. 1991 (Dobson and Vachon, 1994), from the CASP II recovery cruise of May 1992, and from the Sea Truth and Radar

Systems Experiment (STARS'94) of Dec. '94 (Vachon and Dobson,1996). The SAR imagery were processed to the ESA precision image (PRI) standard (ESA/Earthnet, 1992) from RAW signal data on a workstation-based SAR processor at CCRS (MDA, 1995b). The resulting intensity images have L 5 2.9 statistically independent looks with 12.5 m sample spacings in both ground range and azimuth. In **Figure 1**, we have plotted estimates of the kurtosis (a_4) against the skewness-squared (a_3^2) for these SAR images. The observed data are non-Gaussian (i.e. they do not follow the x-squared distribution), but they do seem to be well-modelled by the intensity K-distribution. More detailed analysis of the suitability of the K-distribution, based on Kolmogorov-Smirnov goodness-of-fit tests, supports this assertion (Rey *et al*., 1996). Note that the line representing the K-distribution converges on the appropriate x-squared distribution as $v \to \infty$.

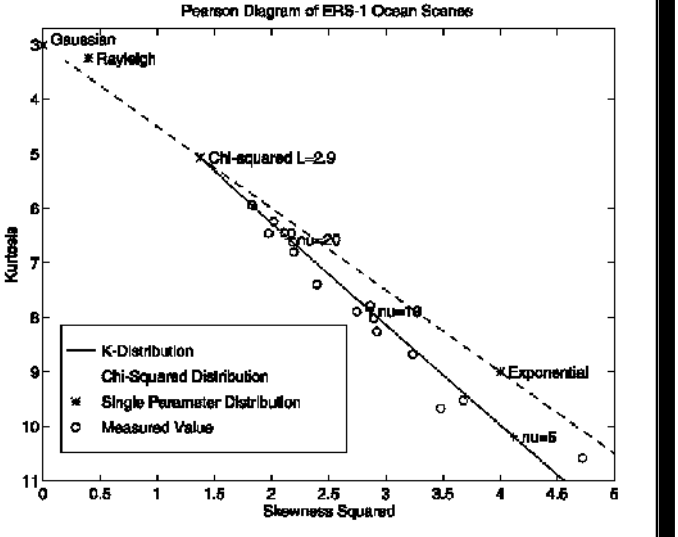

Figure 1.
Pearson diagram of ERS-1 SAR ocean images.

Knowing L, the order parameter may be estimated from the first two moments as follows:

$$\beta = \frac{m_2}{\langle I \rangle^2} = \frac{L + v + 1}{Lv} \tag{10}$$

Other more robust methods of determining v are available (Blacknell, 1994). It is apparent that the K-distribution is a suitable model pdf for our image intensity data and that an appropriate pdf may be completely specified by the image mean, the number of independent looks, and the order parameter, as estimated above.

We consider three separate pdfs for each ship detection scenario. In particular, intensity K-distributions with v = 4, v = 10, and $v = \infty$ (i.e. x-squared). This set of v's should usefully span a realistic set of sea state/wind speed conditions.

It is possible to augment our chosen pdf to include the case of a finite signal-to-noise ratio (SNR) by adjusting the mean value of the pdf by the clutter-to-noise ratio (CNR) (Watts, 1987):

$$I \to \langle I \rangle (1 + 1/\mathrm{CNR}) \quad . \tag{11}$$

This is an imperfect model in the case of the K-distribution when the CNR is small (note that the noise is always Gaussian). However, the case of $v \to \infty$ is more relevant if the CNR is small.

With a useful pdf in hand, it is possible to determine the intensity level which corresponds to an excursion from the mean intensity at a given level of significance. We do this by considering the cumulative pdf:

$$P(I) = \int_0^I p(x)dx \tag{12}$$

where $P(I)$ is the probability that the image intensity is less than I. We can determine if a particular intensity value is significant at a certain level by comparing with the critical image intensity I_c which corresponds to the significance level of interest h_c. This significance level corresponds to a constant false alarm rate of (1 2 h_c) for the pdf of interst. The critical intensity level I_c is given by the solution to

$$\eta_{I_c} = \int_0^{I_c} p(x)dx \tag{13}$$

It is straightforward to determine I_c numerically if the analytic form for $p(x)$ is known. We used h_c = 0.995 as a useful level of significance for this study, though a lower false alarm rate would be required for a practical ship detection system. An analytical solution for equation 13 with a K-distribution has recently been found (Rey *et al*., 1996).

Radar Cross Section of the Ocean

A requirement for this work is a model of the normalized radar cross section s° relevant to RADARSAT's C-band HH polarization radar. This is required for scaling the pdfs used to calculate the ship detection probability. There are not any good physics-based models to draw upon; however there has been considerable effort invested in developing C-band VV polarization models in the context of ERS-1 Scatterometer wind retrieval. A number of models have been developed under the generic name CMOD. The current model for processing archived scatterometer data is termed CMOD5, an empirical model which relates the wind speed, wind direction, and local incidence angle to the normalized radar cross section based upon collocations of scatterometer data and wind vectors from operational buoys (Quilfen, 1993).

We follow the approach of Gower *et al.* (Gower *et al*., 1993) and adjust the cross-section predictions of a C-band VV model with published C-band backscatter polarization ratios (Unal *et al*., 1991). Resulting C-band cross sections for both VV and HH polarizations are plotted for two different wind speeds in **Figure 2**. We note the following:

- The largest s°'s are for upwind directions (i.e. wind blowing towards the radar look direction).
- The smallest s°'s are for (nearly) cross wind directions (i.e. wind blowing across the radar look direction).

- $s°$ increases for increasing wind speed.
- $s°$ for C-band VV is larger than $s°$ for C-band HH for all wind speeds and directions.
- $s°$ for C-band HH decreases more rapidly with increasing incidence angle than $s°$ for C-band VV. They should converge as the incidence angle becomes small.

RADARSAT SAR Parameters

The relevant image modes and parameters are summarized in **Tables 1** and **2** (MDA, 1995a, SPAR, 1993). The tabulated parameters refer to the nominal beam centre for the single beam modes and are all pre-launch values. Operational values for some of these parameters vary slightly (Srivastava *et al*., 1996; SPAR, 1996) (for example the resolutions are better, the number of looks are processor dependent, and the noise floor is lower than was expected), but this will not significantly change the model predictions. If a parameter range is given, the progression is from the near to the far swath edges. (Note: (Raney *et al*., 1991) and (Luscombe *et al*., 1993) provide further information on the radar and its modes of operation.)

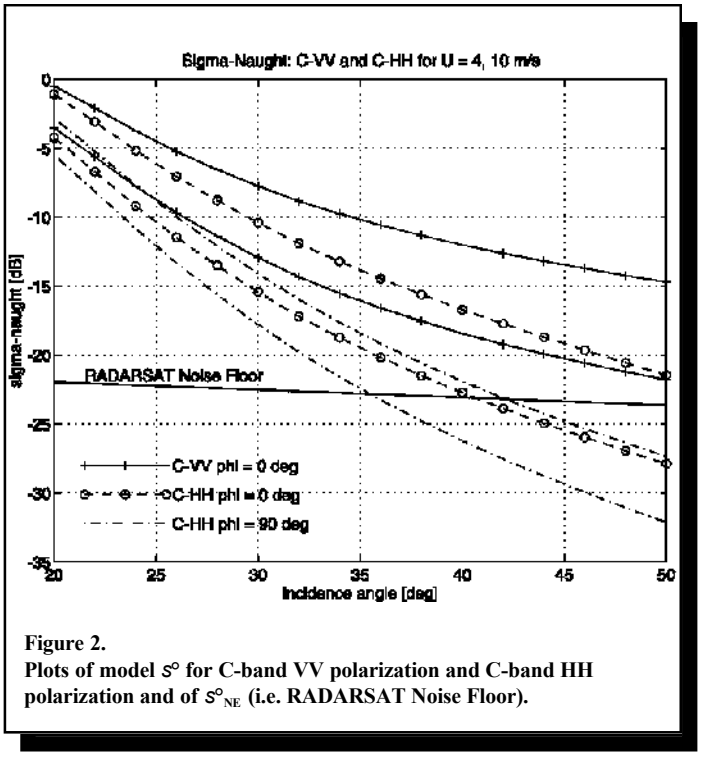

Figure 2.
Plots of model $s°$ for C-band VV polarization and C-band HH polarization and of $s°_{NE}$ (i.e. RADARSAT Noise Floor).

An important parameter for this work is the CNR which can be derived for each beam as the ratio of the modelled normalized radar cross section to the noise-equivalent normalized radar cross section:

$$\mathrm{CNR} = \frac{\sigma°}{s°_{NE}} \qquad (14)$$

A linear fit of $s°_{NE}$ as a function of incidence angle for the RADARSAT SAR is also plotted in **Figure 2**. We see that the CNR (the distance between the $s°$ curve and the $s°_{NE}$ curve, i.e. the RADARSAT noise floor) becomes small as the incidence angle increases and the modelled $s°$ values drop down towards and below the noise floor (depending upon the wind speed and direction).

RADAR CROSS SECTION OF SHIPS

There is rather little information available in the non-classified literature on the relationship between a ship's size and type, and its radar cross section. An empirical formula for grazing incidence angle was published by Skolnik (Skolnik, 1973). The formula scales with radar frequency, is independent of radar polarization and ship orientation, and scales with ship size in proportion to the displacement of the ship measured in tons. Unfortunately, there is not a similar relationship available, empirical or otherwise, for non-grazing incidence angles for a C-band radar. However, Skolnik (Skolnik, 1982) suggests that: "At higher elevation angles, as might be viewed from aircraft, the cross section of ships might be considerably less than at grazing incidence, perhaps by an order of magnitude. When no better information is available, a very rough order of magnitude estimate of the ship's cross section at other-than-grazing incidence can be had by taking the ship's displacement in tons to be equal to its cross section in square meters."

The ship weight in tons (i.e. its radar cross section) may be related to a more tangible measure of ship scale. A regression between ship weight and length for the Bedford Institute of Oceanography (BIO) fleet and for some of the ships participating in the MARCOT '95 exercise provides, as a rule of thumb:

$$s = D = 0.08\, l^{7/3} \quad , \qquad (15)$$

where the units are such that s is the radar cross section of the ship in square meters, D is its displacement in tons, and l is its length in meters.

Now we can determine the detectability of a ship by a SAR on the basis of a ship scale parameter. Knowing the critical image intensity I_c of the relevant pdf (for unity mean image clutter) and the ocean's normalized radar cross section $s°$, we can determine the corresponding minimum point target radar cross section for detection at the chosen probability level as

$$s = I_c\, s°\, r_a r_r \qquad (16)$$

where r_a is the azimuth resolution cell size and r_r is the ground range resolution cell size. The resulting value of s may be directly related to the ship length through equation 15.

Ship Detection Model Results

Sample results from this model for three of the RADARSAT SAR standard beam modes and for the ERS-1 SAR are presented in **Figure 3**. Each plot shows the minimum detectable ship length as a function of the wind speed. Equation 15 can be used to determine the corresponding minimum detectable radar cross section, if that is a preferred parameter. For each plot, the solid lines represent the

Table 1.
Nominal (near beam centre) parameters for RADARSAT SAR single beam modes processed at the RADARSAT Canadian Data Processing Facility and for the ERS-1 SAR.

beam mode	swath [km]	L [looks]	θ [deg]	r_a [m]	r_r [m]	σ°_{NE} [dB]	D_{chirp} [km]
S1	100	3.1	23.5	27	24.2	-23	15.8
S2	100	3.1	27.5	27	20.4	-21	13.6
S3	100	3.1	33.5	27	25.3	-23	11.4
S4	100	3.1	37.0	27	23.4	-23	10.5
S5	100	3.1	39.0	27	22.1	-22	10.0
S6	100	3.1	43.5	27	20.3	-24	9.1
S7	100	3.1	47.0	27	19.1	-23	8.6
F1	50	1	38.5	8.4	8.3	-23	10.1
F2	50	1	40.5	8.4	7.9	-22	9.7
F3	50	1	42.5	8.4	7.6	-23	9.3
F4	50	1	44.5	8.4	7.3	-24	9.0
F5	50	1	46.0	8.4	7.1	-23	8.6
W1	150	3.1	25.5	27	33.8	-22	14.6
W2	150	3.1	35.0	27	24.6	-22	11.0
W3	150	3.1	42.0	27	20.8	-25	9.4
EH1	75	3.1	50.5	27	18	-25	8.1
EH2	75	3.1	51.5	27	17.7	-25	8.0
EH3	75	3.1	53.5	27	17.3	-25	7.8
EH4	75	3.1	55.5	27	16.8	-23	7.6
EH5	75	3.1	57.0	27	16.6	-23	7.5
EH6	75	3.1	58.5	27	16.4	-23	7.3
EL1	170	3.1	16.5	27	39.1	-22	22.2
ERS-1	100	4.9	23.0	30.7	38.4	-24	14.2

S = standard; F = fine; W = wide; EH = extended high incidence; EL = extended low incidence;
L is the number of independent looks; θ is the incidence angle ρ_a is the azimuth resolution;
ρ_r is the ground-range resolution; σ°_{NE} is the noise-equivalent clutter level;
and D_{chirp} is the ground-projected chirp length.

upwind direction (i.e. the largest σ°, hence, worst case) while the dashed lines represent the cross-wind direction (i.e. the smallest σ°, hence, best case). The three curves represent $\nu = 4$, $\nu = 10$ and $\nu = \infty$ from top to bottom (i.e. from worst case to best case).

To facilitate comparison among the various RADARSAT beams and modes, we define a figure-of-merit for ship detection. We propose use of the minimum detectible ship length for $U = 10$ m/s, $\phi = 0°$ (i.e. upwind), and $\nu = 4$. The resulting plot of this ship detection figure-of-merit is shown in **Figure 4**.

From the various individual beam plots and the figure-of-merit plot, the following is evident:

- S1 ship detection performance is better than ERS-1 SAR performance due to the decreased clutter level for HH polarization.
- The ship detection performance improves for increasing incidence angle due to the reduction in clutter level for increasing incidence angle.
- The ship detection performance is best for the fine beam modes due to their large incidence angle and high resolution.
- For ScanSAR modes, the detection performance is best for large incidence angles, but is worse than the standard beam modes due to the larger resolution cell size.
- For larger incidence angles, the ship detection problem becomes the detection of bright point targets against a noise background.

It is apparent that SCNfar, with its 300 km swath, is a good compromise between ship detectibility and swath coverage.

VALIDATION FIELD PROGRAM

A field program was held in March/April 1996 off the coast of Halifax, Nova Scotia to provide quantitative information with which to validate

Table 2.
Nominal parameters for RADARSAT ScanSAR beams.

mode	beams	swath [km]	L [looks]	θ [deg]	r_a [m]	r_r [m]
SCNnear	W1 W2	300	3.5	20–39	47.8 53.8	81.5–43.8
SCNfar	W2 S5 S6	300	3.5	31–46	71.1 71.9 78.8	54.4–38.4
SCW	W1 W2 W3 S7	500	7	20–49	93.1 104.7 117.3 117.5	162.7–73.3

SCN = ScanSAR narrow; SCW = ScanSAR wide. θ and r_r vary as indicated from the near to the far edge of the imaged swath.

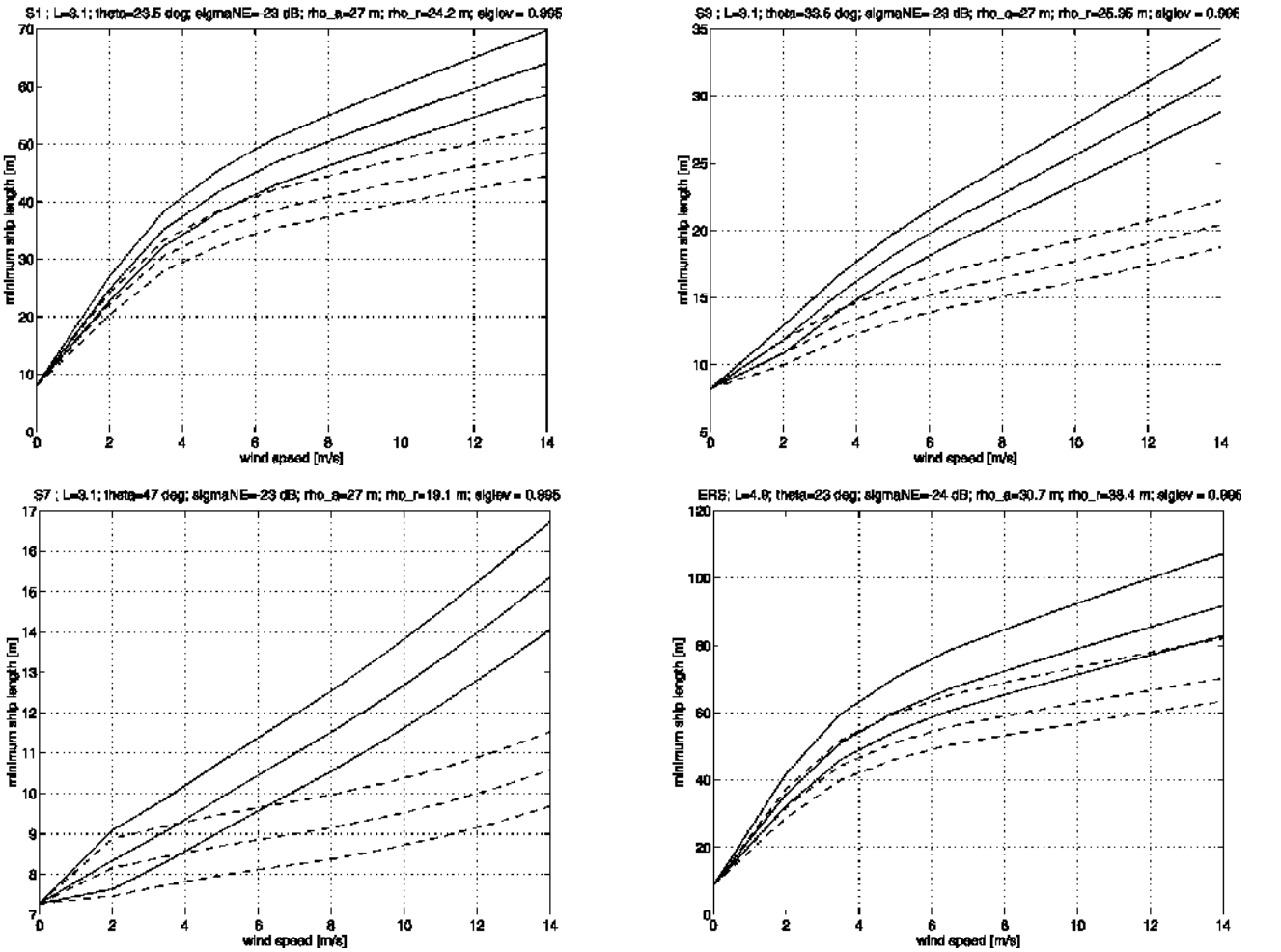

Figure 3.
Minimum detectible ship length for RADARSAT SAR Beams S1 (upper-left), S3 (upper-right), S7 (lower-left), and for ERS-1 SAR (lower-right).

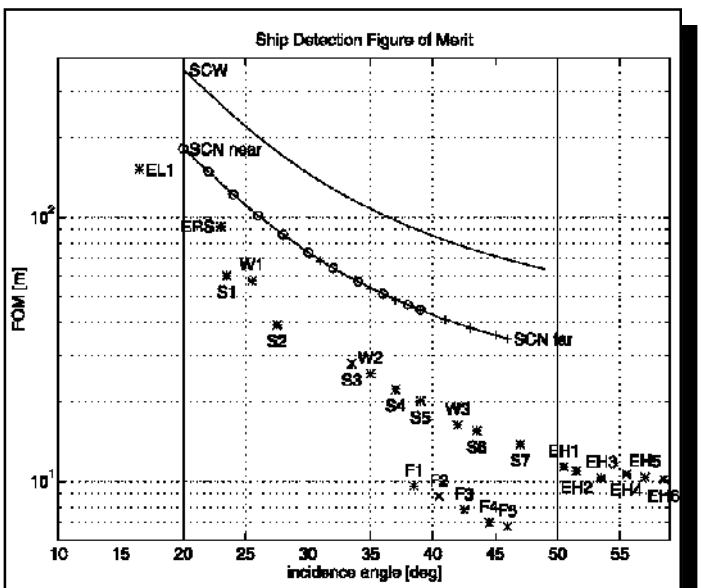

Figure 4.
Plot of the ship detection figure-of-merit for the various beams and modes, as a function of incidence angle.

our ship detection model. There were a number of elements included in the field program, not all of which are discussed here. The activities relevant to this validation include:

- acquisition of wind and wave data from two buoys (MINIMET meteorological buoy and Datawell Directional Wave Rider (DWR) wave buoy) moored near N44.5° W63.0° from 14 March 1996 to 13 April 1996;
- acquisition of 9 RADARSAT SAR scenes in various modes between mid-March and mid-April which included the buoy site, as summarized in **Table 3**;
- the placement of a known ship, as summarized in **Table 4**, near the buoys at the times of the RADARSAT SAR passes; and
- DND Aurora surveillance flights over the area to identify additional ship targets on an opportunity basis.

Other activities during the field program included modelling of the wave conditions, ERS-1 and ERS-2 SAR passes over the buoys, and three CCRS CV-580 underflights of RADARSAT passes. The surface conditions at the RADARSAT pass times are summarized in **Table 5**.

Table 3.
Summary of RADARSAT data from March/April ship detection experiment which are considered in this paper.

Date 1996	Time UTC	Orbit	Track [°true]	Mode	Vessel	CV-580	Aurora
20-March	10:23	1872	195	S3	P	Y	Y
23-March	21:55	1922	345	W1	SF	Y	Y
26-March	22:08	1965	345	S5	WA	Y	Y
27-March	10:18	1972	195	S4	WA	N	Y
30-March	10:31	2015	195	W1	WA	N	N
30-March	21:51	2022	345	S1	WA	N	Y
3-April	10:14	2156	195	W3	WA	N	N
6-April	10:27	2199	195	S3	WA	N	N
9-April	21:59	2249	345	W1	WA	N	N

Table 4.
Vessels participating in the March/April ship detection experiment.

		weight [tons]	length [m]
P	*Parizeau*	1360	65
SF	*Simon Fraser*	1358	62.4
WA	*Sir William Alexander*	3727	83

SAR DATA PROCESSING

The RADARSAT SAR data were obtained through the Canadian Data Processing Facility (CDPF) (Denyer *et al*., 1993, MDA, 1995a) as RAW products. The RAW products were processed to image form using a workstation-based SAR processor at CCRS (MDA, 1995b). The images are similar to the CDPF SGX image standard (MDA, 1995a), but having L=3.7 statistically independent looks with 9 metre pixel spacings in both ground range and azimuth.

RADARSAT SAR Calibration

SAR image data calibration involves interpreting the digital numbers in the processed image file in terms of the radar cross section. Apart from internal system calibration and monitoring procedures (Sheperd and Srivastava, 1993), this process requires knowledge of the geometry, elevation antenna patterns, and a calibration constant (Laur, 1992, for example). Some activities leading to operational RADARSAT SAR calibration have been outlined by Srivastava *et al* (Srivastava *et al*., 1996). Most single beam RADARSAT beam modes will be operationally calibrated in early 1997 (Srivastava *et al*., 1997). In our case, we used the following relationship between the output image and the calibrated cross section:

$$\sigma^{\circ} = \left(\langle I \rangle \frac{R^3}{G^2(\theta)} \right) \frac{\sin \theta}{K} \qquad (17)$$

where $\langle I \rangle$ is the mean image intensity for the region of interest, $G^2(\theta)$ is the two-way elevation antenna pattern gain, R is the range, u is the local incidence angle, and K is the calibration constant. In our processor, $G^2(\theta)$ and R^3 are applied after range compression and before azimuth compression such that squaring and averaging the digital numbers from the processor directly provides the term in brackets in equation 17. The incidence angle correction and calibration constants are then applied directly to the processed image product.

The elevation antenna pattern for each beam mode and the calibration constant were estimated from RADARSAT SAR images acquired over the Amazon rain forest. For rain forest images, we expect that $\gamma^{\circ} = s^{\circ}/\cos\theta = -6.5$ dB for a C-band VV polarization radar, independent of incidence angle (Lecomte and Attema, 1993). This should also apply to RADARSAT's C-band HH polarization radar since the backscatter is primarily from the forest canopy which is composed of branches having random orientation with respect to the incident electromagnetic radiation. An example plot of γ° versus θ for RADARSAT beam S6 is shown in **Figure 5**. By inspection of similar plots for other beam modes, we expect that our resulting RADARSAT calibration is accurate to ±1.0 dB.

Table 5.
Summary of surface conditions at pass times during the March/April ship detection experiment.

Date 1996	Time UTC	$\lvert\vec{U}\rvert$ [m/s]	$\arg\{\vec{U}\}$ [°true]	$T_s - T_a$ [°C]	H_s [m]	s° [dB]	u [°]
20-March	10:23	11.2	92	1.0	1.9	-12.0	32.9
23-March	21:55	6.9	268	-0.7	1.9	-9.1	25.7
26-March	22:08	7.4	208	-1.3	1.0	-21.0	40.6
27-March	10:18	4.9	294	0.2	1.4	-18.3	37.7
30-March	10:31	4.3	353	1.6	0.8	-8.3	22.1
30-March	21:51	8.4	329	-0.3	0.9	-4.1	20.1
3-April	10:13	11.9	314	-1.1	3.0	-14.7	42.0
6-April	10:27	5.7	31	-0.6	0.9	-13.4	27.6
9-April	21:59	1.5	161	-0.6	3.0	-18.3	31.2

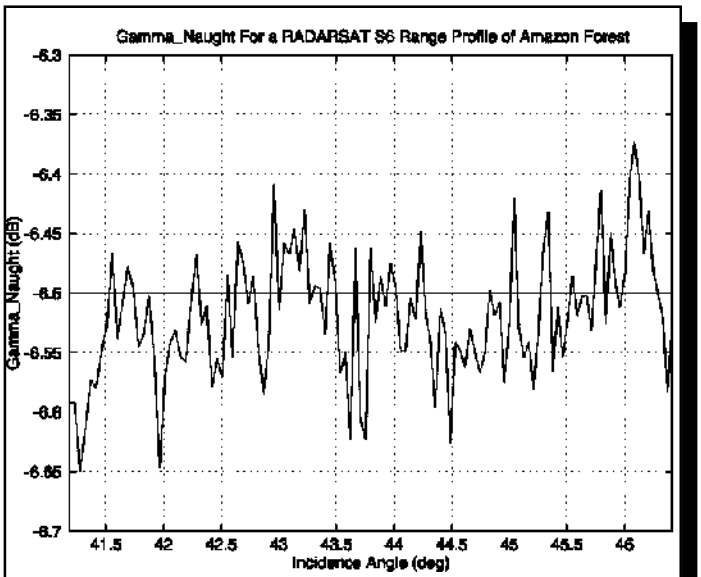

Figure 5.
Plot of γ° versus θ for a RADARSAT SAR beam S6 image of the Amazon rain forest. We expect $\gamma^\circ = s^\circ / \cos\theta$= -6.5 dB in this case.

ADC Saturation

The RADARSAT SAR uses an automatic gain control (AGC) to dynamically adjust the receiver gain for optimal use of the 4-bit analogue-to-digital converter (ADC). Due to the design of the AGC, the gain is set based on the signal power level in the near half portion of the image swath. This means that if the near range contains a low cross section target (such as the ocean at large incidence angles) while the far range contains a higher cross section target (such as land), then the gain may be set too high for the land target, which will result in ADC saturation for the land region.

One effect of ADC saturation is a loss of power coming through the ADC. This effect is illustrated in **Figure 6**. In this beam S4 case, ocean was in the near range and drove the AGC setting. Land was in the far range and was subject to ADC saturation and power loss. The degree of power loss was estimated by measuring the signal data I-channel standard deviation and using the power transfer characteristic of a 4-bit ADC under the assumption of a Gaussian-distributed input signal. It would appear that power loss of greater than 2 dB occurred in this case. After power loss correction, the cross-section profile over the land is seen to be much flatter.

An additional possible effect of ADC saturation is the occurrence of small signal suppression (SSS) (Livingstone *et al*., 1983). In this case, nearby small amplitude signals are suppressed due to the ADC saturation. This effect occurs over the extent of a signal data footprint, which is mode dependent but covers several kilometers in both range and azimuth for RADARSAT. From the coastal region in the figure, it is evident that there is roughly a 1.5 dB power loss at the land boundary. That is, the land cross section has been underestimated by about 1.5 dB. Due to SSS, the opposite side of the boundary must have a similar level of power loss which is maximum at the boundary and reduces to zero one chirp length away from the boundary. That is, the cross section of the water is similarly underestimated. The ground-range chirp length at beam centre D_{chirp} for RADARSAT's nominal 42 *m*s chirp duration (37 μs for ERS-1), corresponding to 6.3 km slant-range chirp length, is included in **Table 1**.

Due to the way in which the AGC is set, we expect that we will not have power loss problems for open ocean data. If land is in the near range, then the gain could be too small over the ocean, leading to the potential of ADC underflow rather than overflow. On the other hand, if ocean is in the near range, the gain would be appropriately set. However, there could be ADC power loss over coastal land. A less obvious effect is SSS in the very near coastal zone. We suggest that RADARSAT SAR calibration always be treated with caution for such regions, especially if closer to shore than one chirp length.

VALIDATION OF MODEL ASSUMPTIONS

In this section we validate some of the ship detection model assumptions using our calibrated RADARSAT SAR data. In particular, we show that there is excellent agreement between the observed RADARSAT SAR cross sections and those predicted by the hybrid model. Furthermore, the K-distribution is shown to be a suitable pdf for RADARSAT SAR ocean images. We also show that our very simple ship length-dependent cross section model is within the correct order of magnitude.

Hybrid s° Model

As discussed above, the hybrid C-band HH polarization ocean clutter model we used is composed of C-band VV polarization radar cross sections from CMOD5, adjusted to HH cross sections using measured polarization ratios. We can validate the

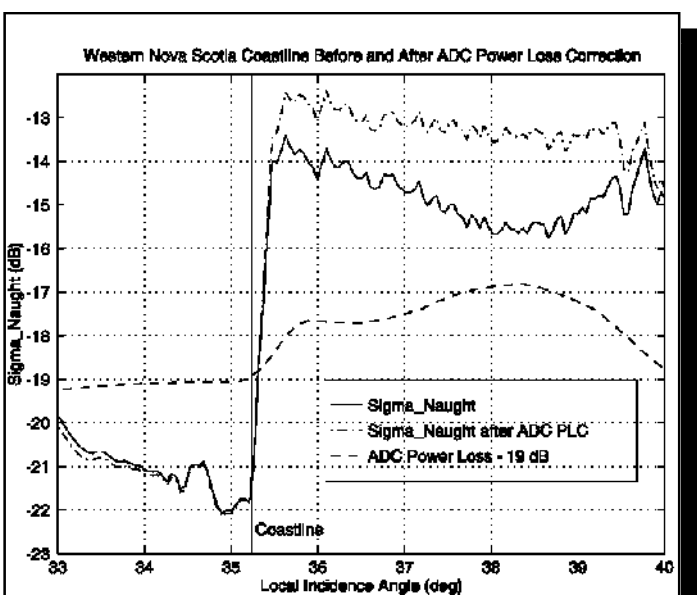

Figure 6.
Plots of σ° versus θ for a RADARSAT SAR beam S4 image covering open ocean and land over the west coast of Nova Scotia. The effects of ADC saturation power loss and its compensation for the land region are illustrated.

suitability of this model by comparing calibrated RADARSAT SAR cross-section profiles with cross-section profiles from the model driven by the *in situ* wind speed measurements taken by the MINIMET buoy and collocated in space and time with the RADARSAT passes. For this purpose, the winds were corrected to a measurement height of 10 m using a standard log profile, allowing for wind speed variations with air stability (see **Table 5**). Example calibration and hybrid model results are shown in **Figure 7**. From the four example profiles shown, it is evident that, in each case, there is good agreement between the RADARSAT and model profiles, especially in the vicinity of the measurement location. The agreement is good in terms of both the absolute cross section level and the slope of the curve with increasing incidence angle.

To further illustrate this point, in **Figure 8**, we present a scatter plot of observed σ°, as measured from the RADARSAT SAR data at the buoy location, against hybrid model σ° predictions driven by the measured local wind speed. The data are seen to be very well-correlated for the available 9 cases over nearly 20 dB of dynamic range. There are 3 out-liers for the lower cross section cases which may be correlated with dynamic conditions (e.g. a nearby atmospheric front) or the presence of a nadir ambiguity near the buoy location. It is important to note that the correlation is best for the larger cross section (higher wind speed) cases.

K-distribution

The ship detection model used a K-distribution for the image pdf. The validity of this model pdf for RADARSAT data was tested by plotting measured kurtosis against skewness-squared from a homogeneous region in the vicinity of the buoy location. The resulting RADARSAT Pearson diagram is shown in **Figure 9**. It can be seen that the RADARSAT SAR data are well-clustered about the K-distribution with L=3.7 independent looks. The values for the K-distribution order parameter v for the available 9 cases are larger than those for the ERS-1 SAR data considered previously, probably due to the larger number of independent looks for the RADARSAT images. However,

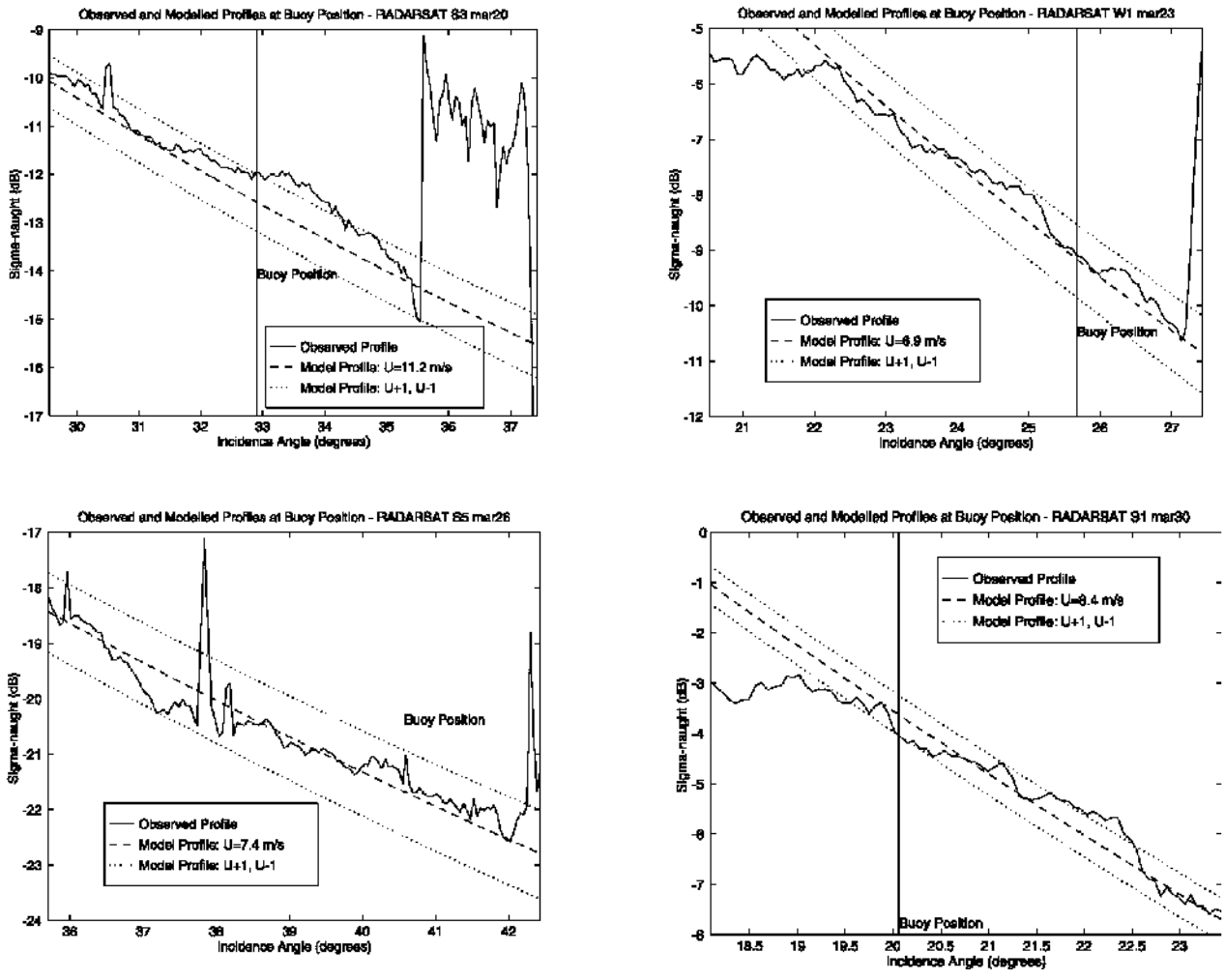

Figure 7.
Plots of s° versus u for some RADARSAT SAR ocean images, with dates and modes as indicated in the plot titles. The smooth curves are the hybrid C-band HH model s° profiles for the measured wind vectors. Note that some of the image profiles contain both land and water and nadir ambiguities.

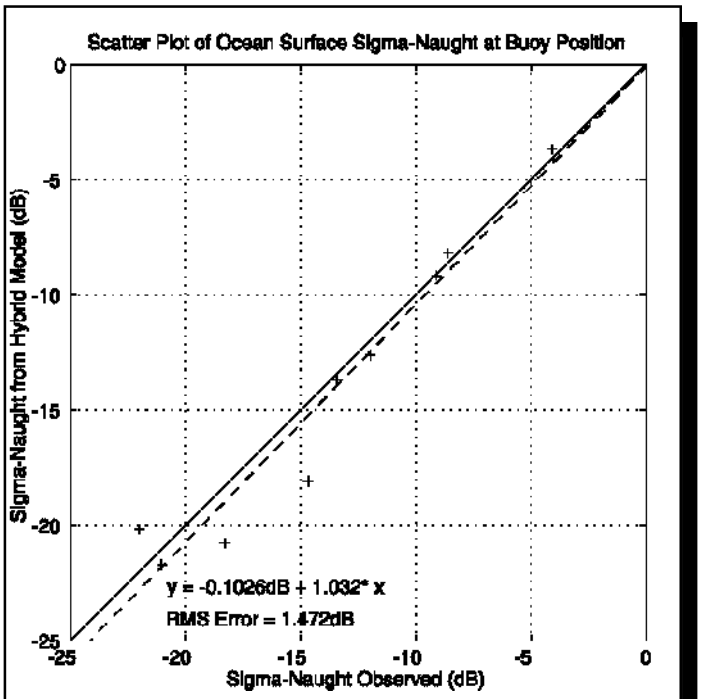

Figure 8.
Scatter plot of C-band HH hybrid model s° driven by *in situ* wind vector measurements and observed RADARSAT SAR s°.

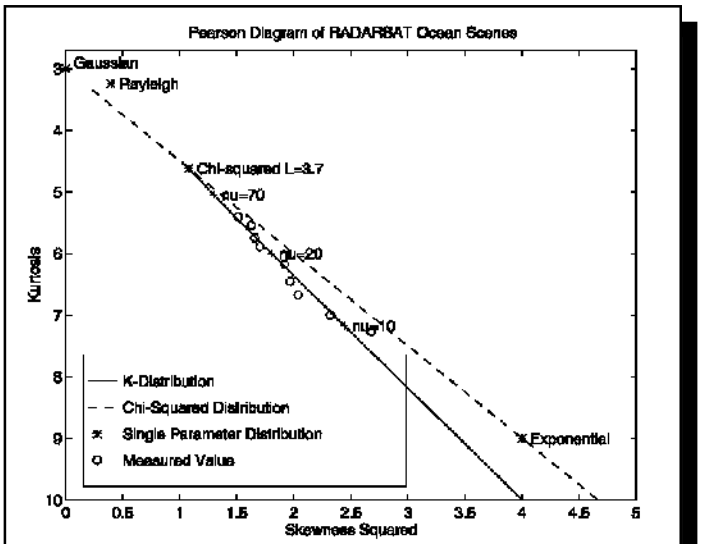

Figure 9.
Pearson diagram of RADARSAT SAR ocean images.

the range of order parameter values are still within the bounds of those chosen for the ship detection model runs.

Radar Cross Section of Ships

We measured the ship cross section directly from the calibrated image data by integrating over the region around the ship and then subtracting the clutter contribution which was estimated from the surrounding clutter pixels. An example W3 signature for *Sir William Alexander* is shown in **Figure 10**. We considered 8 known ship cases (in the April 9 case, the known ship was masked by a nadir ambiguity) along with vessels identified with high confidence from the Aurora surveillance flights. In **Figure 11**, we plot the anomaly between the measured cross section and the parametric cross section model of equation 15, as a function of incidence angle.

Recall that the cross section used in our detection model was based on Skolnik's assumption about ship weight and cross section and that we used a simple regression formula between ship weight and length. For the ships considered, we find that our simple relationship is within 10 dB, but that the anomaly tends to increase with increasing incidence angle. This is illustrated by the dashed line in the figure. Although we have not considered ship orientation at all in this analysis, use of the best fit line to our data allows recovery of the vessel length to within 20 % based on the measured ship cross section alone. It is apparent that our simple model will tend to underestimate the ship cross section, and therefore underestimate the ship detectibility. Obviously, many more known ship cases should be analysed in order to derive a better understanding of the radar cross section of ships, especially as a function of incidence angle and relative ship heading.

CONCLUSIONS

In this paper, we have presented a statistical model which provides predictions of RADARSAT SAR performance for ship detection. The model includes ocean clutter, image pdf, and ship cross section elements. The ocean clutter and image pdf were derived from previous experience with ERS-1 SAR data. The model results are summarized in the figure-of-merit plot shown in **Figure 4**. It is apparent that SCNfar represents a good compromise between ship detectibility and swath coverage.

A ship detection field program, carried out off the coast of Halifax, Nova Scotia in March/April 1996 has provided RADARSAT SAR data with excellent *in situ* wind and wave data, along with image signatures of known ships. The RADARSAT data were processed to image form and calibrated using Amazon rain forest images to derive elevation antenna patterns and a calibration constant. Our RADARSAT SAR image calibration is accurate to ±1.0 dB. Note that, due to the operation of RADARSAT's automatic gain control, analogue-to-digital converter saturation power loss is possible under some circumstances, but is most severe over land if ocean occurs in the near half swath. Clearly this is not an issue for scenes of interest for ship detection. On the other hand, small signal suppression could lead to underestimation of the radar cross section in near coastal regions.

We have successfully validated some of the key ship detection model assumptions using the calibrated RADARSAT and *in situ* field program data acquired in March/April 1996. In particular, we showed that our hybrid C-band HH polarization cross section model is excellent for the conditions encountered and that the K-distribution is a suitable pdf for RADARSAT ocean scenes. Furthermore, we showed that our simple model for ship cross section, which was based upon the ship length alone, is within the correct order of magnitude, although it tends to underestimate the

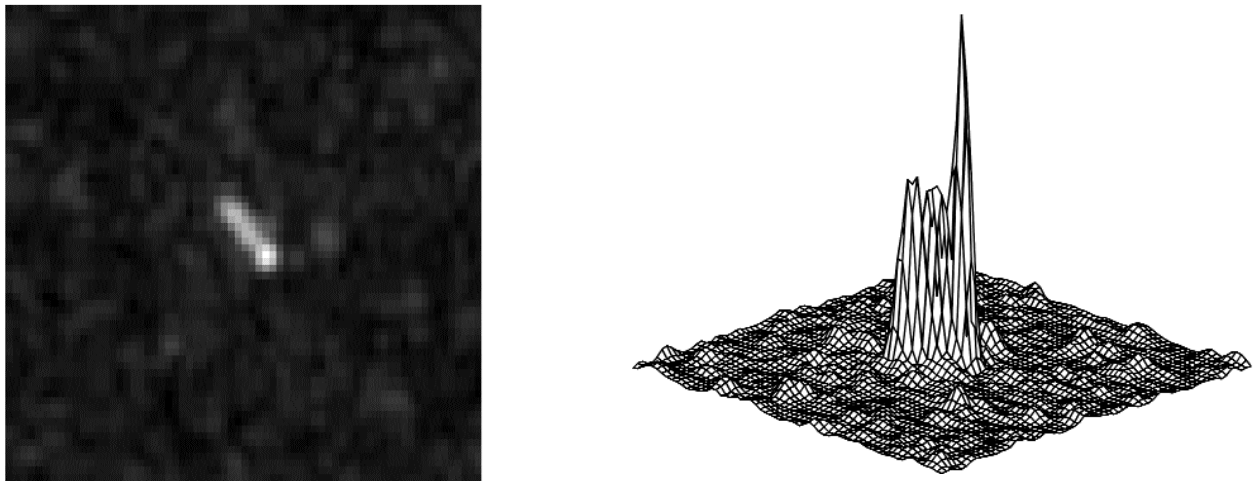

Figure 10.
Example RADARSAT SAR W3 image signature of *Sir William Alexander* as image amplitude and mesh plots from the 6 April '96 pass.

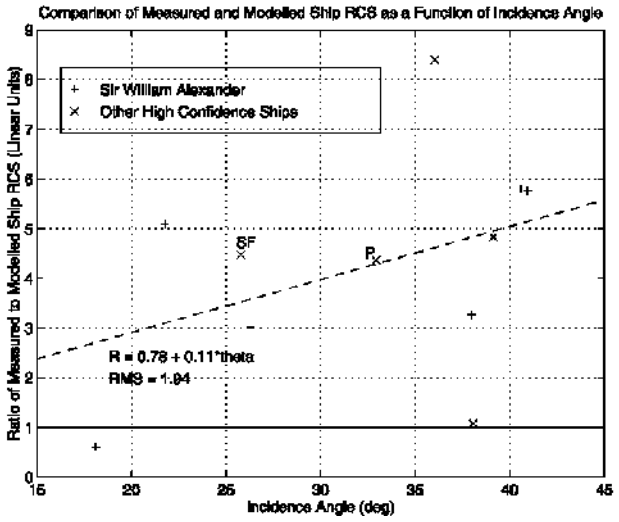

Figure 11.
Plot of ship radar cross-section anomaly (ratio of measured to model cross sections) versus u as measured for known ships in RADARSAT SAR images. All values would be close to unity (solid line) if the Skolnik rule-of-thumb were correct. The dashed line is the best linear fit to the data points as a function of incidence angle.

ship cross section especially with increasing incidence angle. The ship cross section model is such that the detection model has underestimated the ship detectibility by RADARSAT for most cases. We do not yet have adequate data to address the incidence angle and relative ship heading dependence in any useful detail.

The results of validating our RADARSAT SAR ship detection model using actual RADARSAT data are excellent. However, further work is required to better quantify RADARSAT's ship detection performance. In particular, observations of more ships of a variety of sizes would be very helpful, as would observations taken under high wind and wave conditions. Additional field work in support of these objectives was carried out in the winter of 1996/97.

An element of the operational utilization of RADARSAT SAR data is the Ocean Feature Workstation (OFW) (Olsen *et al*., 1995) which is installed at CCRS's Gatineau Satellite Station. One function of the OFW is ship detection, including wake analysis (Rey *et al*., 1990; Rey *et al*., 1993). The results of this study will be used to improve the OFW ship detection algorithms which should serve to better demonstrate the operational use of RADARSAT SAR data for ship detection.

ACKNOWLEDGEMENTS

We were assisted in the RADARSAT data processing and analysis by Adeel Ahmad and Jonathon Bailey (CCRS/UWaterloo coop program) and in the *in situ* data processing by Chantal Allard (BIO/UDalhousie coop program). The *in situ* data processing was supported by PERD project 6B2018. The RADARSAT data from the field program were obtained under RADARSAT ADRO Project 143 and RVP. We thank Laurence Gray (CCRS), Chuck Livingstone (CCRS), Ridha Touzi (CCRS), Howard Edel (MEDS), Tony Luscombe (SPAR), Stu Smith (BIO), Paul Lim (MDA), and Terje Wahl (NDRE) for helpful discussions. We thank Bob Hawkins (CCRS), Tom Lukowski (CCRS), John Wolfe (CCRS) and Linda Takken (CCRS/UWaterloo coop program) for helping us with the RADARSAT data calibration and CSA and RSI for supplying the calibration data sets as part of a wider calibration effort being conducted by CSA. The Vessel Operations Centre (Dartmouth) of the Canadian Coast Guard deployed and recovered the buoys, supplied a ship near the buoy site at the times of the RADARSAT passes, and provided harbour traffic information. The Department of National Defence, through LtCmdr. Jim Day, provided Aurora surveillance information for the RADARSAT passes in March 1996. Ilya Kushniruk (CCG) provided information on specific vessels.

REFERENCES

Blacknell, D., "Comparison of parameter estimators for K-distribution", *IEE Proc.-Radar, Sonar Navig.,* 141(1), pp. 45-52, 1994.

Chapron, B., R. Garello, V. Kerbaol, and J. Lefevre, "Nonlinear theory of ocean-SAR transformation and statistical analysis of ERS-1 SAR-wave mode imagettes", *Proc. Second ERS-1 Symposium - Space at the Service of our Environment*, Hamburg, Germany, 11-14 October 1993, ESA SP-361, pp. 247-250, 1994.

Denyer, N., R.K. Raney, and N. Shepherd, "The RADARSAT SAR data processing facility", *Canadian Journal of Remote Sensing*, 19(4), pp. 311-316, 1993.

Dobson, F.W., and P.W. Vachon, "The Grand Banks ERS-1 SAR wave spectra validation Experiment: Program overview and data summary", *Atmosphere-Ocean*, 32(1), pp. 7-29, 1994.

Eldhuset, K., "An automatic ship and ship wake detection system for spaceborne SAR images in coastal regions", *IEEE Trans. Geoscience Rem. Sens*., 34(4), pp. 1010-1019, 1996.

ESA/Earthnet, "ESA ERS-1 Product Specification", Technical Report ESA SP-1149, ESA Publications Division, ESTEC, Noordwijk, The Netherlands, 1992.

Freeman, N.G., A.L. Gray, R.K. Hawkins, and C.E. Livingstone, "CCRS Convair 580 results relevant to ERS-1 wind and wave calibration", *Proc. Workshop on ERS-1 Wind and Wave Calibration*, Schliersee, FRG, 2-6 June 1986, ESA SP-262, pp. 101-109, 1986.

Gower, J.F.R., P.W. Vachon, and H. Edel, "Ocean applications of RADARSAT", *Canadian Journal of Remote Sensing*, 19(4), pp. 372-383, 1993.

Gray, A.L., R.K. Hawkins, and C.E. Livingstone, "A simple model for satellite SAR radiometric discrimination estimation", *Proc. 8th Canadian Symposium on Remote Sensing*, Montreal, Quebec, 3-6 May 1983, pp. 25-38, 1984.

Laur, H., "Derivation of backscattering coefficient s° in ERS-1.SAR.PRI products", Technical Report ESA/ESRIN, Issue 1, Rev. 0, European Space Agency, 1992.

Lecomte, P., and E.P.W. Attema, "Calibration & validation of the ERS-1 wind scatterometer", *Proc. 1st ERS-1 Symp., Space at the Service of our Environment*, 4-6 Nov. 1992, Cannes, France, ESA SP-359 Vol. 1, pp. 19-29, 1993.

Livingstone, C.E., D. Hudson, J.D. Lyden, C. Liskow, R. Shuchman, and R. Lowry, "Gain compression effects in SAR imagery", *Proc 17th International Symposium on Remote Sensing of the Environment,* 9-13 May 1983, Ann Arbour, U.S.A., pp. 1109-1116, 1983.

Luscombe, A.P., I. Ferguson, N. Shepherd, D.G. Zimcik, and P. Naraine, "The RADARSAT synthetic aperture radar development", *Canadian Journal of Remote Sensing,* 19(4), pp. 298-310, 1993.

MDA, *RADARSAT - Canadian Data Processing Facility Data Products Manual* CDRL No. MN-2, MacDonald Dettwiler, 13800 Commerce Parkway, Richmond, B.C., Canada V6V 2J3, RZ-MA-50-5309, 1995a.

MDA, *Scientific desktop SAR processing System - Operations Manual,* MacDonald Dettwiler, 13800 Commerce Parkway, Richmond, B.C., Canada V6V 2J3, ML-MA-50-7048, 1995b.

Oliver, C.J., "Optimum texture estimators for SAR clutter", *J. Physics:* D, pp. 1824-1835, 1993.

Olsen, R.B., P. Bugden, Y. Andrade, P. Hoyt, M. Lewis, H. Edel, and C. Bjerkelund, "Operational use of RADARSAT SAR for marine monitoring and surveillance", *Proc. 1995 International Geoscience and Remote Sensing Symposium (IGARSS'95)*, 10-14 July 1995, Firenze, Italy, IEEE 95CH35770, pp. 224-226, 1995.

Quilfen, Y., "ERS-1 off-line wind scatterometer products", Technical Report ERS-SCAT/IOA/DOS-01, IFREMER, 1993.

Raney, R.K., A.P. Luscombe, E.J. Langham, and S. Ahmed, "RADARSAT", *Proc. IEEE*, 79(6), pp. 839-849, 1991.

Rey, M.T., A. Drosopoulos, and D. Petrovic, "A search procedure for ships in RADARSAT imagery", Technical report, Defence Research Establishment Ottawa, Ottawa, Ontario, Canada, 1996.

Rey, M.T., J.K. Tunaley, J.T. Folinsbee, P.A. Jahans, J.A. Dixon, and M.R. Vant, "Application of Radon transform techniques to wake detection in Seasat-A SAR images", *IEEE Trans. Geoscience Rem. Sens.*, 28(4), pp. 553-560, 1990.

Rey, M.T., J.K.E. Tunaley, and T. Sibald, "Use of the Dempster-Shafer algorithm for the detection of SAR ship wakes", *IEEE Trans. Geoscience Rem. Sens.*, 31(5), pp. 1114-1118, 1993.

Shepherd, N.W., and S.K. Srivastava, "Radiometric gain stabilization in the RADARSAT SAR", *Proc. 18th Canadian Symposium on Remote Sensing*, 7-10 June 1993, Sherbrooke (Quebec), Canada, pp. 381-386, 1993.

Skolnik, M.I., "An empirical formula for the radar cross section of ships at grazing incidence", *IEEE Trans. Aerospace Elect. Syst*., 10, pp. 66, 1973.

Skolnik, M.I., *Introduction to Radar Systems*, McGraw-Hill Book Company, New York, NY, U.S.A., 1982.

SPAR, RADARSAT - Critical Design Review, Space Segment, 1993.

SPAR, RADARSAT I - Space Segment Commissioning Review, 1996.

Srivastava, S.K., R.K. Hawkins, and T.I. Lukowski, "Operational calibration for RADARSAT data", *Proc. International Symposium: Geomatics in the Era of RADARSAT (GER'97)*, 25-30 May 1997, Ottawa, Canada, To appear, 1997.

Srivastava, S.K., T.I. Lukowski, R.K. Hawkins, C. Cloutier, L.D. Teany, N.W. Shepherd, R.B. Gray, A.P. Luscombe, and R. Bank, "RADARSAT calibration: The operational system and initial results", *Proc. 1996 International Geoscience and Remote Sensing Symposium* (IGARSS'96), 27-31 May 1996, Lincoln, U.S.A., pp. 1290-1292, 1996.

Tack, R.E., and D. Nazarenko, "RADARSAT - A new view of the world", *Proc. Oceanology International '96, The Global Ocean - Towards Operational Oceanography,* 4-6 March 1996, Brighton, England, Vol. 2, pp. 285-292, 1996.

Trunk, G.V., and S.F. George, "Detection of targets in non-Gaussian sea clutter", *IEEE Trans. Aerospace Elect. Syst.,* 6(5), pp. 620-628, 1970.

Unal, C. M.H., P. Snoeij, and P.J.F. Swart, "The polarization-dependent relation between radar backscatter from the ocean surface and surface wind vector at frequencies between 1 and 18 GHz", *IEEE Trans. Geoscience Rem. Sens.,* 29(4), pp. 621-626, 1991.

Vachon, P.W., "Ship Detection by the RADARSAT SAR (A Working Paper)", Technical report, Canada Centre for Remote Sensing, Ottawa, Ontario, Canada, Draft, 1995.

Vachon, P.W., and F.W. Dobson, "Validation of wind vector retrieval from ERS-1 SAR images over the ocean", *The Global Atm. and Ocean Syst.*, 5, pp. 177-187, 1996.

Vachon, P.W., H.E. Krogstad, and J.S. Paterson, "Airborne and spaceborne synthetic aperture radar observations of ocean waves", *Atmosphere-Ocean*, 32(1), pp. 83-112, 1994.

Wahl, T., K. Eldhuset, and Å. Skøelv, "Ship traffic monitoring using the ERS-1 SAR", *Proc. First ERS-1 Symposium - Space at the Service of our Environment*, Cannes, France, 4-6 November 1992, ESA SP-359, pp. 823-828, 1993.

Watts, S., "Radar detection prediction in K-distributed sea clutter and thermal noise", *IEEE Trans. Aerospace Elect. Syst.*, 23(1), pp. 40-45, 1987.